

Synthesis of binary Sb_2E_3 (E = S, Se) and ternary $\text{Sb}_2(\text{S,Se})_3$ Nanowires using *tailor-made* Single-Source-Precursors

Stefan Heimann,^[a] Wilfried Assenmacher,^[b] Oleg Prymak,^[a] and Stephan Schulz*^[a]

Abstract: Thermal decomposition of four *single source precursors* of the type $(\text{Et}_2\text{Sb})_2\text{E}$ and Et_3SbE (E = S, Se) at 170 °C in the presence of suitable capping agents yielded binary Sb_2S_3 and Sb_2Se_3 nanowires. In addition, simultaneous decomposition of $(\text{Et}_2\text{Sb})_2\text{S}$ and $(\text{Et}_2\text{Sb})_2\text{Se}$ gave the ternary phase $\text{Sb}_2(\text{S,Se})_3$ with almost equal S and Se concentrations. The materials were characterized by XRD, REM, EDX, ED and HRTEM.

Introduction

Group 15/16 chalcogenides of the general type M_2E_3 (M = Sb, Bi; E = S, Se, Te) have a long standing history in material sciences. Sb_2S_3 for instance is of particular interest for technical applications in sensitized solar cells (SSCs) due to its attractive bandgap energy (~1.7 eV) and high extinction coefficient ($1.8 \times 10^5 \text{ cm}^{-1}$) in the visible region, allowing the fabrication of heterojunction solar cells with over 5% of power conversion efficiency under 1 sun = 1 kWm^{-2} illumination.^[1] Moreover, Sb_2S_3 is of potential interest for ferroelectric phase transition. The stibnite-type structure of Sb_2S_3 favors the ferroelectric phase transition as was shown by theoretical calculations.^[2] The ferroelectric phase transition of Sb_2S_3 at 420 K is caused by the structural change from $Pnma$ (D_{2h}^{16}) to $Pna2_1$ (C_{2v}^9).^[3] More recently, Sb_2S_3 was shown to have a promising technical application as battery material.^[4] Antimony selenide Sb_2Se_3 is a pnictogen chalcogenide semiconductor with ~1 eV bandgap,^[5] which exhibits a high Seebeck coefficient^[6] with a fast amorphous crystalline transition,^[7] rendering it very attractive for technical applications in photovoltaic,^[8] phase change memory^[9] and in thermoelectric (TE) devices.^[10] TE materials are of particular interest since they allow the interchange of thermal energy and electricity for the utilization of waste heat and for cooling. Although many promising TE materials have been discovered in recent years, antimony and bismuth chalcogenide-based materials still belong to the most widely used.

Bulk Sb_2Se_3 shows a 6- to 9-fold higher Seebeck coefficient $S \sim 1800 \mu\text{V/K}$ ^[11] than the best bismuth telluride alloys,^[12] but its technical application in TE devices is hampered by its low

electrical conductivity of $\sigma \sim 10^{-6}\text{-}10^{-2} \Omega^{-1}\text{m}^{-1}$,^[11,13] resulting in a low TE power factor $S^2\sigma$. Increasing σ in Sb_2Se_3 while retaining a low thermal conductivity κ is therefore of particular interest. Nanostructuring has been shown to be a suitable approach for realizing a high thermoelectric figure of merit zT since it allows to some extent the decoupling of thermal and electrical conductivity due to the different lengths scales of the mean free path of electrons and phonons.^[14] Moreover, doping of the material was shown to allow an increase of the figure of merit zT .^[15] For instance, Mehta et al. reported on the microwave-activated solvothermal synthesis of one-dimensional sulfurized orthorhombic Sb_2Se_3 nanowires and nanotubes with enhanced electrical conductivity. Sulfur-capping of the nanocrystal surfaces resulted in $10^4\text{-}10^{10}$ higher electrical conductivity and about 10-fold higher charge carrier mobility in the one-dimensional nanocrystal compared to the respective bulk value.^[16] Moreover, selenium-alloyed^[17] and sulfur-doped Bi_2Te_3 nanoparticles^[18] as well as quaternary $(\text{Sb,Bi})_2(\text{Se,Te})_3$ nanocrystals^[19] and nanostructured heterocomposite materials such as $\text{Bi}_2\text{Te}_3/\text{Bi}_2\text{S}_3$ ^[20] and $\text{Bi}_2\text{Te}_3/\text{Bi}_2\text{Se}_3$ ^[21] have also been shown to exhibit improved TE properties due to a decoupling of the variables mentioned before. As a consequence, bottom-up chemistry approaches are currently investigated in detail in order to either generate property-defined phase separation of multicomponents on multiple length scales or to generate simultaneously two different nanomaterials in order to create bulk TE materials.^[22]

Various types of Sb_2S_3 nanostructures have been synthesized and characterized.^[23] Sb_2E_3 (E = S, Se) nanowires were prepared by use of polyol processes,^[24] solvothermal routes,^[16,25] and gas-induced reduction routes,^[26] respectively. Moreover, Sb_2S_3 nanowires were fabricated within cylindrical pores of anodic alumina (AAO) templates ($\text{Sb}_2\text{S}_3\text{-AAO}$) by a solvent-free technique utilizing $\text{Sb}(\text{S}_2\text{CNEt}_2)_3$,^[27] while sea urchin-like Sb_2S_3 materials assembled to nanorods were prepared by a glucose-assisted reduction route.^[28] In addition, thin films of these materials were deposited by *atomic layer deposition* (ALD)^[29] and *aerosol-assisted chemical vapor deposition* (AACVD) processes.^[30] Recently, the promising potential of so-called *single-source precursors* for the synthesis of nanostructured M_2E_3 materials was demonstrated.^[1,8,30,31] Moreover, Kim et al. synthesized Sb_2Te_3 nanoplates by thermal decomposition of Ph_2SbTeR (R = Et, Ph) at 300 °C,^[32] while our group reported on the solution-based synthesis of highly stoichiometric, crystalline Sb_2Te_3 nanoparticles^[33] and on MOCVD-grown (*metal organic chemical vapor deposition*) Sb_2Te_3 thin films by use of $(\text{Et}_2\text{Sb})_2\text{Te}$ as *tailor-made single source precursor*.^[34] The Sb_2Te_3 nanoparticles showed much lower thermal conductivity (0.29 to 0.27 W/m·K) compared to that of single crystalline Sb_2Te_3 , for which values of 1.6 W/(m·K) and 5.6 W/(m·K) at ambient temperature have been reported.^[35]

[a] Faculty of Chemistry and Center for Nanointegration Duisburg-Essen (CENIDE), University of Duisburg-Essen, Universitätsstr. 5-7, 45117 Essen, Germany
Fax: + 49 201-1834635
E-mail: stephan.schulz@uni-due.de
Homepage: http://www.uni-due.de/ak_schulz/

[b] Institute of Inorganic Chemistry, University of Bonn, Römerstr. 164, 53117 Bonn, Germany

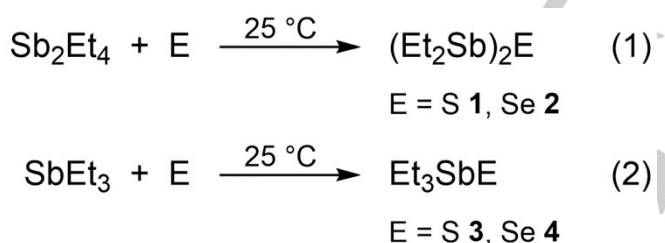
Supporting information for this article is given via a link at the end of the document.

Moreover, both the nanoparticles and the thin films exhibited rather high Seebeck coefficients between 145 $\mu\text{V}/\text{K}$ and 170 $\mu\text{V}/\text{K}$, which are close to optimize values of bulk materials,^[36] demonstrating a low defect density and low carrier densities in the order of 10^{19} to 10^{20} cm^{-3} . In addition, low defect Sb_2Te_3 thin films were grown by ALD using SbCl_3 and $\text{Te}(\text{SiEt}_3)_2$.^[37]

We became interested in the development of suitable *single source precursors* for the synthesis of the corresponding binary Sb_2E_3 materials as well as for ternary materials or heterocomposite materials by simultaneous thermolysis reactions, which requires well balanced thermal properties of the precursors. Herein, we report on four *single source precursors* of the type $(\text{Et}_2\text{Sb})_2\text{E}$ and Et_3SbE ($\text{E} = \text{S}, \text{Se}$), which were successfully used for the wet-chemical synthesis of Sb_2S_3 and Sb_2Se_3 nanowires at temperatures below 180 $^\circ\text{C}$. The influence of the solvent (DIPB, oleylamine) and the capping agent (PVP*) on the morphology, chemical composition and crystallinity of the resulting binary nanomaterials was investigated. Simultaneous decomposition of two different precursors of the type $(\text{Et}_2\text{Sb})_2\text{E}$ ($\text{E} = \text{S}, \text{Se}$) yielded the ternary material phase $\text{Sb}_2(\text{S},\text{Se})_3$.

Results and Discussion

$(\text{Et}_2\text{Sb})_2\text{S}$ **1** and $(\text{Et}_2\text{Sb})_2\text{Se}$ **2**^[42] were synthesized by a slightly modified reaction as reported by *Breunig et al.*^[43] and Et_3SbS **3** and Et_3SbSe **4**^[39] were prepared by oxidative addition reaction of elemental sulfur and selenium to Et_3Sb .^[44,45]



Scheme 1. Synthesis of **1** - **4**.

$(\text{Et}_2\text{Sb})_2\text{S}$ **1** and $(\text{Et}_2\text{Sb})_2\text{Se}$ **2** are yellow liquids, which start to decompose at 100 $^\circ\text{C}$. DSC experiments of $(\text{Et}_2\text{Sb})_2\text{E}$ ($\text{E} = \text{S}$ **1**, Se **2**) and Et_3SbE ($\text{E} = \text{S}$ **3**, Se **4**) were performed to investigate their thermal stability (SI). Even though distibanylsulfanes $(\text{R}_2\text{Sb})_2\text{S}$ were found to decompose with formation of SbR_3 and Sb_2S_3 ,^[46] the decomposition mechanisms of **1** and **2** are more complex compared to that of $(\text{Et}_2\text{Sb})_2\text{Te}$, which decomposes in a stoichiometric reaction with formation of Sb_2Te_3 and SbEt_3 .^[40] The thermolysis of **1** and **2** was also investigated by *in situ* ^1H NMR spectroscopy, clearly proving the formation of SbEt_3 , which decomposes at almost 300 $^\circ\text{C}$, as well as SEt_2 and SeEt_2 . SEt_2 decomposes at almost 420 $^\circ\text{C}$, while SeEt_2 shows a lower decomposition temperature of roughly 370 $^\circ\text{C}$ due to the weaker Se-C bonds compared to S-C bonds. The formation of SEt_2 and

SeEt_2 most likely occurs through a radical mechanism. In addition, several additional peaks in the ^1H NMR spectra point to the formation of so far unidentified reaction products (SI) and a more complex reaction mechanism. Et_3SbS **3** and Et_3SbSe **4** are colorless crystalline solids with melting points of almost 130 $^\circ\text{C}$ as is shown by endothermic peaks in the DSC curves. Almost immediately after melting, the resulting slightly yellow liquids start to decompose with formation of black solids and SbEt_3 , which starts to decompose at about 300 $^\circ\text{C}$. The decomposition of **3** and **4** also proceed with formation of SEt_2 and SeEt_2 , respectively, which then decompose at higher temperatures, as well as other so far unidentified products.

Synthesis of Sb_2S_3 nanoparticles. Heating a yellow solution of $(\text{Et}_2\text{Sb})_2\text{S}$ **1** or a light orange suspension of Et_3SbS **3** in DIPB and PVP* at 170 $^\circ\text{C}$ for 10 h yielded black dispersions, from which black crystalline solids were isolated by centrifugation after addition of 10 mL of MeOH. In contrast, heating a suspension of **3** in DIPB and PVP* at 130 $^\circ\text{C}$ for 10 h gave a red suspension, from which a red precipitate was isolated after addition of methanol (Fig. 1).^[47] XRD confirmed that the red precipitate is amorphous and EDX studies showed an Sb:S molar ratio of 42.1:57.1 at%, which is close to the expected value for Sb_2S_3 (40:60 at%), as well as some carbon (about 3 at%). Additional heating of either the isolated red precipitate at 200 $^\circ\text{C}$ for 4 h as well as the red suspension for additional 4 h at 160 $^\circ\text{C}$ yielded a black solid, that was isolated as described before. According to these findings, the thermolysis temperature of 130 $^\circ\text{C}$ is below the required phase transition temperature for crystalline Sb_2S_3 .



Figure 1. Pictures of the red colored dispersion of amorphous Sb_2S_3 formed at 130 $^\circ\text{C}$ in DIPB and of the black colored dispersion of crystalline Sb_2S_3 after additional heating at 160 $^\circ\text{C}$.

The red Sb_2S_3 nanoparticles show an amorphous-to-crystalline phase transition (red/black) at temperatures higher than 140 $^\circ\text{C}$, which agrees well with previous studies (160 $^\circ\text{C}$).^[47] In contrast, Tiekink and White reported on the synthesis of Sb_2S_3 particles by thermolysis of different *single source precursors* in water and ethylene glycol at 120 $^\circ\text{C}$, 160 $^\circ\text{C}$ and 200 $^\circ\text{C}$, respectively, and observed the characteristic color change from red to black at significantly higher temperatures (200 $^\circ\text{C}$),^[30] whereas *Wang et al.* obtained crystalline Sb_2S_3 by hydrothermal treatment of $\text{K}_2[\text{Sb}_2(\text{C}_4\text{H}_4\text{O}_6)]$, CTAB and thioacetamide at 155 $^\circ\text{C}$.^[48] Moreover, *Son et al.* obtained crystalline Sb_2S_3 nanowires by reaction of SbCl_3 and elemental sulfur in oleylamine at 175 $^\circ\text{C}$.^[49]

The black solids as-obtained from precursors **1** and **3** are crystalline Sb_2S_3 materials as was shown by XRD (SI, Fig S5, S7). All Bragg peaks with a significant intensity can be indexed on the basis of the structure of orthorhombic Sb_2S_3 , whereas no crystalline impurities attributable to antimony, sulfur, or Sb_2O_3

could be detected. No significant texture for the Sb_2S_3 nanowires was observed; only a slightly higher intensity in [001] orientation was detected. Comparing to the theoretical XRD pattern of Sb_2S_3 orthorhombic structure, the experimental XRD peaks 103 and 015 were roughly 20-30 % higher as the 100%-Peak 112. All other peaks correspond very well to the theoretical intensity distribution (Fig. 2).

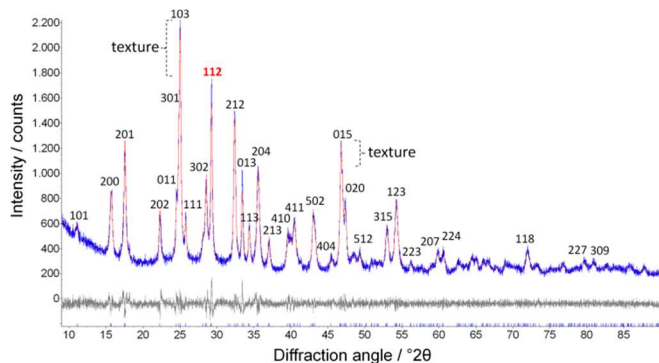


Figure 2. X-ray diffractogram (with profile and difference plot from Rietveld refinement, $R_{wp} = 5.9$) of the Sb_2S_3 nanowires as obtained with precursor **3** at 170 °C in DIPB/PVP* solution; the most intense peaks with 100%-peak 112 as well as textured peaks 103 and 015 are labeled.

The calculated lattice parameters (a : 1.134(1) nm, b : 0.384(1) nm, c : 1.125(1) nm; standard setting $Pnma$) are in a very good agreement with the ICDD database for the pure orthorhombic Sb_2S_3 phase. Using the Rietveld refinement, the crystallographic density of the material ($\rho_{XRD} = 4.61 \text{ g/cm}^3$) was calculated (SI Table S1). SEM analysis showed the formation of Sb_2S_3 nanobundles and flower-like structures (Fig. 3), which are slightly sulfur-deficient (Sb:S = 42:58 at%) according to EDX analysis. However, the nanobundles as-obtained from precursor **1** show a slightly more distinguished nanowire substructure compared to those obtained with **3**.

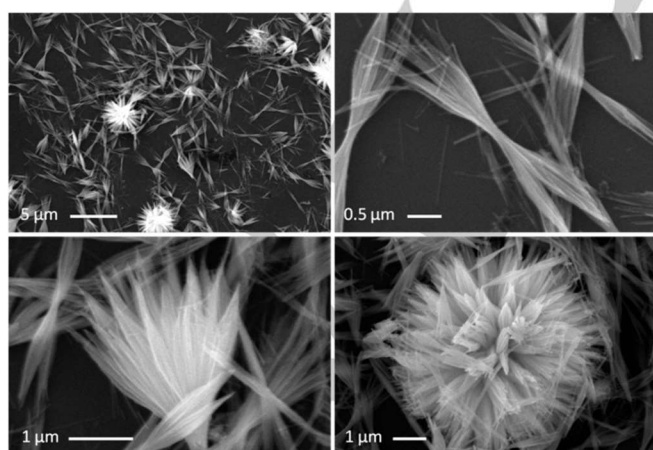


Figure 3. SEM photographs of Sb_2S_3 nanowires, nanobundles and flower-like structures as-obtained with precursor **1** (top) and **3** (bottom) in DIPB/PVP* solution at 170 °C.

These results were confirmed by TEM studies (Fig. 4). The crystalline Sb_2S_3 nanobundles are as long as 5 μm and show diameters below 150 nm in the middle. In addition to the nanobundles, single nanowires were observed. Sb_2S_3 (stibnite) crystallizes orthorhombic in space group 62 with lattice parameters of a : 1.131 nm, b : 0.383 nm and c : 1.123 nm using the standard setting $Pnma$.

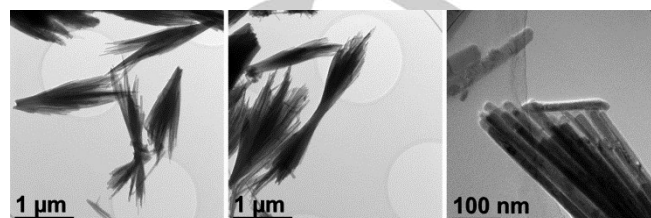


Figure 4. TEM micrographs of Sb_2S_3 nanobundles and wires formed with precursor **1** in DIPB/PVP* solution at 170 °C.

The growth direction of the nanowires was revealed from high resolution TEM (HRTEM) images (Fig. 5). The spacings perpendicular to the nanowire axis are 0.38 nm and correspond to the d -values of {010}, which is the b lattice parameter. The spacings parallel to the wire axis are 0.565 nm matching d_{200} . The FFT indicates that this Sb_2S_3 nanowire is in [001] orientation, which is consistent with the XRD results. All d -values measured in the FFT are in good agreement with stibnite data taken from ICDD database.^[50] Thus, the growth direction of these 1D crystals is along $\langle 010 \rangle$, which is the shortest of the lattice parameters. The stibnite structure consists of chains of edge sharing, square pyramidal SbS_5 -units running along the short lattice parameter, which might be the explanation for the growth in this direction. Electron diffraction of an area covered by several bundles shows powder ring patterns (debyeograms, SI, Fig S9a), which agree very well with simulated data from stibnite, proving the material to be pure and crystalline.

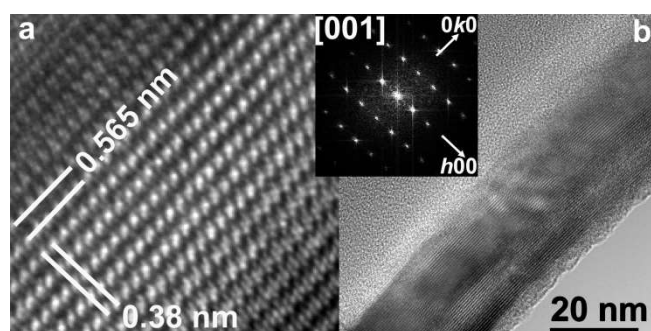


Figure 5. HRTEM image (b) of a single Sb_2S_3 nanowire as-obtained with precursor **1** in DIPB/PVP* solution at 170 °C in [001] orientation. Zoom (a) and amplitude of FFT as inset.

The growth of the nanobundles, which was previously reported by Wang *et al.* and Pei *et al.*,^[26,28,48] most likely occurs through a

mechanism recently postulated by *Chen et al.*^[51] using a hydrothermal growth process. PVP molecules preferentially bind to facets of the initially formed Sb_2S_3 crystal seeds, enhancing the anisotropic growth along the direction of the 0.38 nm lattice parameter. As-formed nanowires then aggregate to as-observed nanobundles.

In order to investigate the role of the solvent and the capping agent in more detail, thermolyses of **1** and **3** were also performed in oleylamine as well as in DIPB in the absence of PVP*. While thermolyses of **1** and **3** in oleylamine (OA) only yielded amorphous materials even at elevated temperatures (180 °C), thermolyses of **1** and **3** at 170 °C in DIPB in the absence of PVP* resulted again in the formation of crystalline Sb_2S_3 . Fig. 6 shows the formation of large, flower-like crystals with diameters of up to 700 nm, which is significantly thicker compared to the Sb_2S_3 nanomaterial formed in the presence of PVP*. These results clearly demonstrate the strong binding affinity of PVP* to the (100) facets of the Sb_2S_3 crystal seeds.

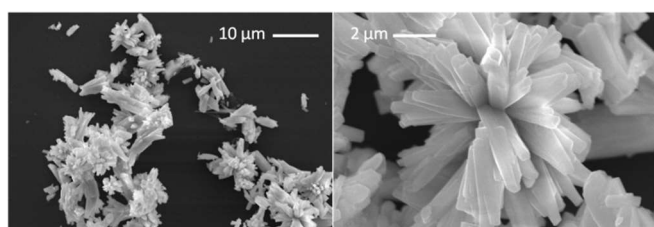


Figure 6. SEM photographs of Sb_2S_3 flower-like structures formed with precursor **3** in DIPB at 170 °C.

Synthesis of Sb_2Se_3 nanoparticles. Heating a solution of $(\text{Et}_2\text{Sb})_2\text{Se}$ **2** in either oleylamine or DIPB/PVP* at 170 °C for 10h yielded black dispersions, from which black solids were isolated after addition of 10 mL of MeOH. Powder X-ray diffraction (SI, Fig S6) proved the formation of crystalline Sb_2Se_3 materials based on the structure of orthorhombic Sb_2Se_3 . Fig. 7 shows SEM photographs of the material as-obtained with **2** at 170 °C in DIPB/PVP*, proving the formation of Sb_2Se_3 nanowires and elemental antimony, which is visible as small cubic crystals. The Sb_2Se_3 nanowires are up to 5 µm in length and show diameters between 20 to 100 nm, while the cubic Sb nanoparticles show an average edge length of 600 nm. SEM photographs of the material as-obtained by thermolysis of **2** in OA at 150 and 170 °C is given in the supplement (SI, Fig S10).

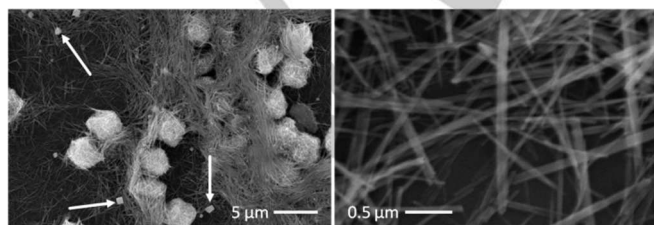


Figure 7. SEM photographs of Sb_2Se_3 nanowires formed with precursor **2** in DIPB/PVP* solution at 170 °C.

Fig. 8 shows TEM bright field images of the Sb_2Se_3 nanowires as-obtained from precursor **2** in a solution of DIPB/PVP* at 170 °C. Only a very few Sb crystals are present as small cubes visible at low magnifications. The nanowires have a big aspect ratio with lengths up to 5 µm and diameters of 20-30 nm. They are covered by an amorphous seam. From EDX analysis no other elements than Sb, Se, C and some O are found in the wires and in the seam. From contrast it may be suggested, that the seam consists of hydrocarbons.

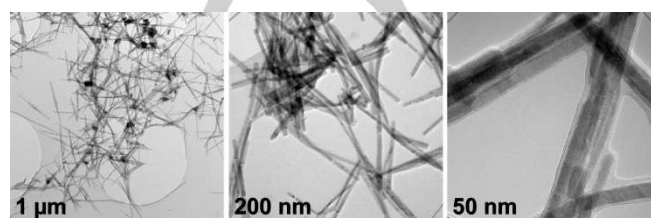


Figure 8. TEM micrographs of Sb_2Se_3 nanowires formed with precursor **2** in DIPB/PVP* solution at 170 °C.

The growth direction of the Sb_2Se_3 nanowires is along the $\langle 010 \rangle$ direction of the stibnite structure in $Pnma$ setting. Fig. 9 shows HRTEM images of an Sb_2Se_3 nanowire with lattice fringes of (010) planes ($d_{010} = 0.396 \text{ nm}$ ^[52]) perpendicular and spacings of (200) planes ($d_{200} = 0.5885 \text{ nm}$) parallel to the growth direction. FFT of the HRTEM images show by d-values and symmetry the orientation of the crystal as [001], where the {00} row points in the growing direction. Ring patterns of the diffracted intensity of several crystals (SI, Fig S9b) are in good agreement with simulated data of Sb_2Se_3 without any intensities from impurities.

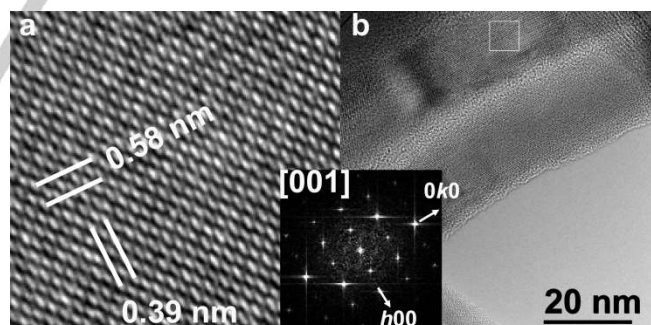


Figure 9. Zoom (a) and amplitude of FFT as inset of the boxed area in the HRTEM image (b) of Sb_2Se_3 nanowires formed with precursor **2** in DIPB/PVP* solution at 170 °C in [001] orientation.

Thermolyses of Et_3SbSe **4** at 170 °C in either DIPB or in DIPB/PVP* only yielded Sb_2Se_3 nanowires contaminated with small amounts of elemental Sb, whereas its decomposition in OA at either 150 or 170 °C gave nearly phase-pure Sb_2Se_3 (Fig. 10). No significant texture of the Sb_2Se_3 nanowires was observed, probably due to the statistical distribution of the nanowires in all directions. The determined lattice parameters

(*a*: 1.179(1) nm, *b*: 0.398(1) nm, *c*: 1.164(1) nm; standard setting *Pnma*) were in a very good agreement with the ICDD database for the pure orthorhombic Sb_2Se_3 phase. The crystallographic density of the material ($\rho_{\text{XRD}} = 5.85 \text{ g/cm}^3$) was also determined (SI Table S1). However, the Sb_2Se_3 material also contains small amounts of crystalline Sb (roughly 0.25 wt.% according to a Rietveld refinement) as was shown by XRD (Fig. 10) and by EDX analyses, which proved the formation of a slightly Sb-rich Sb_2Se_3 phase (Sb:Se = 42:58 at%).

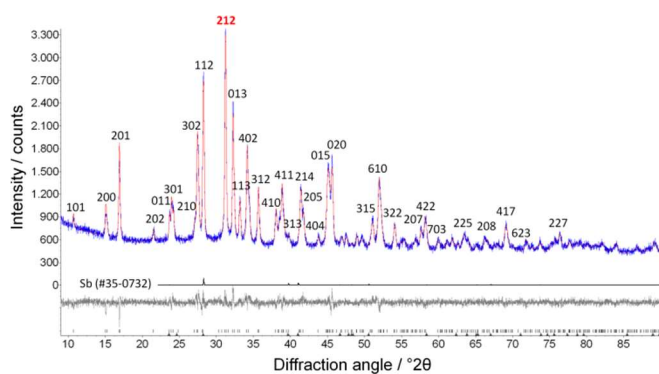


Figure 10. X-ray diffractogram (with profile and difference plot from Rietveld refinement, $R_{\text{wp}} = 4.4$) of the black solid as obtained with precursor **4** at 150 °C in OA. The most intense peaks with 100%-peak 212 of Sb_2Se_3 are labeled; a very small amount of Sb is shown.

The up to 5 μm long nanowires show diameters between 50 and 200 nm (Fig. 11), which is somewhat bigger compared to those obtained by a polyol process (30 - 50 nm).^[25] EDX analyses of the materials synthesized at 150 and 170 °C clearly proved the formation of almost pure Sb_2Se_3 (Sb:Se molar ratios of 41:59 at%). The material obtained with precursor **4** in DIPB and PVP* showed larger agglomerates of Sb_2Se_3 nanowires compared to those obtained in OA at 150 °C.

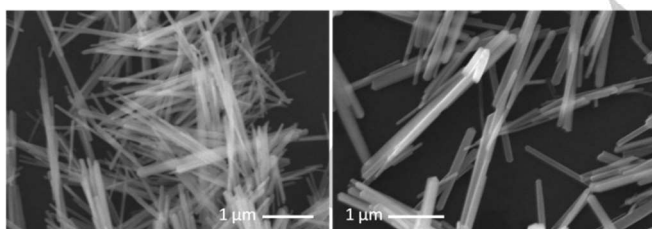


Figure 11. SEM photographs of Sb_2Se_3 nanowires formed with precursor **4** in OA at 150 °C (left) and 170 °C (right).

The reason for the formation of Sb-contaminated Sb_2Se_3 by thermolysis of $\text{Et}_3\text{SbSe 4}$ in DIPB and PVP* at 170 °C can't be explained by thermal decomposition of SbEt_3 , which is formed upon thermolysis of **4**, since SbEt_3 decomposes at temperatures higher than 280 °C.^[32] Therefore, we propose that the elemental Sb is formed by decomposition of small Sb_2Se_3 nanoparticles, in which Sb^{3+} is formally reduced to Sb^0 and Se^{2-} is oxidized to Se^0 .

The larger agglomerates always contained slightly Se-rich materials, which further supports this proposed mechanism. Nielsch et al. reported comparable findings for Bi_2Te_3 nanowires, which became Te-deficient with increasing temperature (150 – 400 °C).^[53] At 400 °C, the Bi_2Te_3 nanowires were completely transferred into Bi_4Te_3 nanowires, which can also be described as $(\text{Bi}_2)(\text{Bi}_2\text{Te}_3)$. Since an analogous Sb-rich Sb_4Se_3 phase doesn't exist, the additional Sb forms elemental Sb cubes, while the Se is most likely present as amorphous selenium within the material.

Synthesis of ternary $\text{Sb}_2(\text{S,Se})_3$ nanoparticles. Ternary alloys of $\text{Sb}_2\text{Se}_{3-x}\text{S}_x$ ($0 < x < 3$) may have composition-dependent bandgap energies. Moreover, they show lower lattice thermal conductivities and better efficiency in solar energy conversion than the binary compounds as a result from disorder-induced phonon scattering processes.^[54] Unfortunately, the synthesis of one-dimensional (1D), ternary $\text{Sb}_2\text{Se}_{3-x}\text{S}_x$ nanowires is still difficult although various methods have been developed for the fabrication of one-dimensional Sb_2S_3 and Sb_2Se_3 nanostructures. Deng et al reported on the synthesis of crystalline $\text{Sb}_2\text{Se}_{3-x}\text{S}_x$ nanotubes ($x = 0 - 3$) by reaction of Sb(III)-2-ethylhexanoic acid (EHA) complex with S and Se in paraffin liquid at elevated temperatures.^[25a] The optical bandgap energy of the as-synthesized $\text{Sb}_2\text{Se}_{3-x}\text{S}_x$ ($0 \leq x \leq 3$) nanotubes was found to increase with increasing sulfur concentration from 1.18 (Sb_2Se_3) to 1.63 eV (Sb_2S_3), respectively.

Simultaneous decomposition of a solution containing equimolar amounts of **1** and **2**, whose thermal properties are very similar (SI Fig S1, S2), in DIPB/PVP* at 170 °C was investigated to prove the possible formation of a ternary $\text{Sb}_2(\text{S,Se})_3$ material phase. Workup of the resulting dispersion gave a black crystalline precipitate, which contains almost equal amounts of sulfur and selenium according to EDX analysis (Sb:S:Se = 42:28:30).

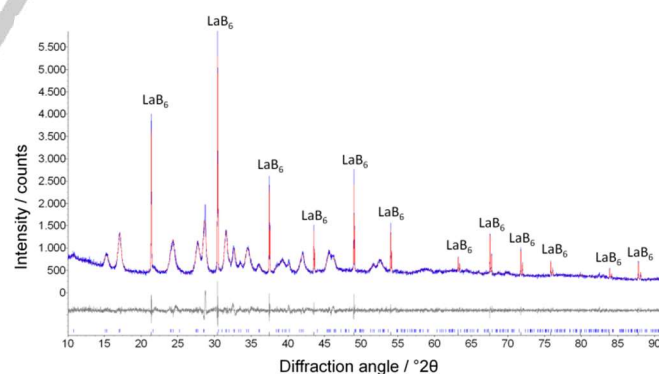


Figure 12. X-ray diffractogram (with profile and difference plot from Rietveld refinement; $R_{\text{wp}} = 5.2$) of $\text{Sb}_2(\text{S,Se})_3$ nanowires formed by simultaneous decomposition of **1** and **2** in DIPB/PVP* at 170 °C with the microcrystalline standard LaB_6 (the corresponding sharp peaks are denoted).

These results agree very well with the XRD results and Rietveld refinement, showing the formation of a ternary $\text{Sb}_2(\text{S,Se})_3$ phase with the substitution range of 51.7% S and 48.3 % Se. For exact determination of the sample displacement and for an accurate

calculation of the lattice parameters of the $\text{Sb}_2(\text{S,Se})_3$ phase, the powder sample was mixed with about the same amount of LaB_6 (Fig. 12). The lattice parameters of the substituted $\text{Sb}_2(\text{S,Se})_3$ phase (a : 1.151(1) nm, b : 1.166(1) nm, c : 0.392(1) nm; setting $Pbnm$) correspond very well to those reported by Moustafa *et al.*^[55] Moreover, the microstrain of the ternary material increased to 0.18 % (comparing to previous 0.05 % and 0.09 % for pure Sb_2S_3 and Sb_2Se_3 correspondently) as a result from the substitution of S^{2-} by bigger Se^{2-} anions and the following change of the unit cell. The crystallographic density of the ternary material ($\rho_{\text{XRD}} = 5.14 \text{ g/cm}^3$) was also determined (SI Table S1). These results were confirmed by TEM studies, according to which the material consists of $\text{Sb}_2(\text{S,Se})_3$ nanowires up to 3 μm in lengths and 30 - 50 nm in diameter (Fig. 13). Neither an amorphous seam nor any impurities were observed in the TEM pictures and in the diffracted rings of the nanowires (SI, Fig S9c).

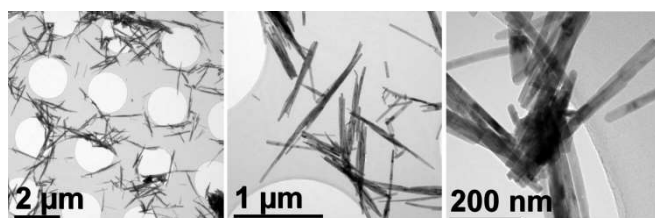


Figure 13. TEM pictures of $\text{Sb}_2(\text{S,Se})_3$ nanowires as-obtained from simultaneous decomposition of **1** and **2** in DIPB/PVP* at 170 °C.

The $\text{Sb}_2(\text{S,Se})_3$ nanowires again grew along the $\langle 010 \rangle$ direction ($d_{010} = 0.39 \text{ nm}$) of the $\text{Sb}_2(\text{S,Se})_3$ stibnite structure ($Pnma$).^[54] Fig. 14 shows a HRTEM image recorded at 250 keV of the $\text{Sb}_2(\text{S,Se})_3$ nanowire, in which the growth direction is indicated by a double arrow-headed line. The lattice spacings perpendicular to the growth direction, as well as the FFT, that can be indexed as $[101]$, prove the growth direction.

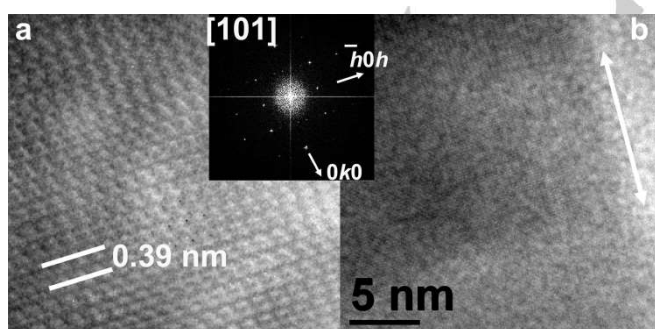


Figure 14. Zoom (a) and amplitude of FFT as inset of the HRTEM image (b) of $\text{Sb}_2(\text{S,Se})_3$ nanowires formed by simultaneous decomposition of **1** and **2** in DIPB/PVP* at 170 °C in $[101]$ orientation.

All $\text{Sb}_2(\text{S,Se})_3$ nanowires are single crystalline and spot EDX analyses reveal the presence of Sb, S and Se within the wires,

whose homogeneous distribution within the several nanowires was proven by EDX line-scans (Fig. 15). Apart from the lacking quality of these EDX data, resulting from the short acquisition times that could be used due to specimen drift and contamination, the line-scan analysis reveals doubtless that the $\text{Sb}_2(\text{S,Se})_3$ nanowires are a solid solution crystals.

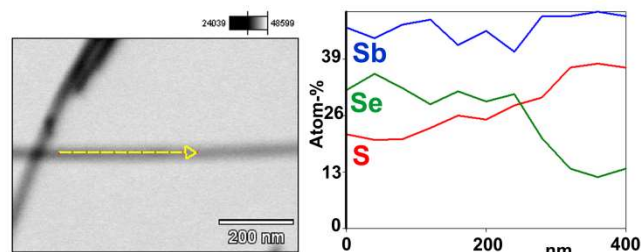


Figure 15. Scanning TEM image and EDX line-scans of a $\text{Sb}_2(\text{S,Se})_3$ nanowire.

Conclusions

Binary antimony chalcogenide nanowires Sb_2E_3 ($\text{E} = \text{S, Se}$) were obtained by thermal decomposition of four tailor-made single source precursors of the general type $(\text{Et}_2\text{Sb})_2\text{E}$ and Et_3SbE ($\text{E} = \text{S, Se}$) in DIPB/PVP* at mild reaction conditions ($T = 170 \text{ }^\circ\text{C}$). In addition, simultaneous decomposition of equimolar amounts of $\text{S}(\text{SbEt}_2)_2$ and $\text{S}(\text{SbEt}_2)_2$ yielded ternary $\text{Sb}_2(\text{S,Se})_3$ nanowires without any sign of the formation of biphasic material mixtures. The materials were fully characterized by various techniques including XRD and TEM.

Experimental Section

Materials. Sulfur, selenium, oleylamine and Poly(1-vinylpyrrolidone)-*graft*-1-hexadecene (PVP*, CAS 136445-69-7) were used as received and 1,3-diisopropylbenzene (DIPB) was carefully dried over Na/K alloy and degassed prior to use. **1** to **4** were prepared according to literature methods.^[39,42] Solvents were dried over Na/K and degassed. All synthetic steps were done in a glovebox under Ar atmosphere.

Synthesis of binary Sb_2E_3 nanomaterials by thermal decomposition of **1 - **4**.** 0.20 g of the precursor (**1** - **4**) were added to a freshly prepared solution of 0.25 g PVP* in 10 mL of diisopropylbenzene (DIPB) at ambient temperature. Heating to 170 °C for 10 h yielded black dispersions, from which black precipitates were isolated by centrifugation after addition of 10 mL of methanol. Repeated re-dispersion in CHCl_3 (3 times) in an ultrasonic bath, precipitation (MeOH) and centrifugation under Ar atmosphere yielded pure materials.

Co-thermolysis of $(\text{Et}_2\text{Sb})_2\text{S}$ and $(\text{Et}_2\text{Sb})_2\text{Se}$. 0.10 g of precursor **1** and 0.10 g of the precursor **2** were added to a freshly prepared solution of 0.25 g PVP* in 10 mL of DIPB at ambient temperature. Heating to 170 °C for 10 h yielded black dispersions, from which black precipitates were isolated by centrifugation after addition of 10 mL of methanol. Repeated re-dispersion in CHCl_3 (3 times) in an ultrasonic bath, precipitation (MeOH) and centrifugation under Ar atmosphere yielded pure material.

Thermal Analysis. DSC studies were performed on a Netzsch Phox 200 machine (heating rate 2 °C min⁻¹).

SEM Analysis. SEM studies were carried out either on an ESEM Quanta 400 FEG or a Jeol JSM 6510 equipped with an energy dispersive X-ray spectroscopy (EDX) device (Bruker Quantax 400).

TEM Analysis. TEM studies were conducted on transmission electron microscopes (i) FEI Philips CM30 T/LaB₆ operated at 250 kV and (ii) FEI-Philips CM300 UT/FEG operated at 300 kV. Both microscopes are equipped Gatan CCD's for image recording and with Thermo NSS systems for EDX analysis using a Si(Li) Nanotracer and a HP-Ge EDX detector, respectively. The samples were prepared on perforated carbon foils supported by a copper grid without further grinding. For simulation of TEM data the java version of EMS was used.^[40]

X-ray Analysis. XRD patterns were obtained using a Bruker D8 Advance powder diffractometer with Cu K_α radiation (λ: 1.5418 Å, 40 kV and 40 mA) using a silicon single crystal as sample holder to minimize scattering. For better homogenization, the dried powder samples were re-dispersed in ethanol on the silicon surface and then investigated in the range from 10 to 90° 2θ with a step size of 0.01° 2θ with a counting time of 0.6 s. Rietveld refinement was performed with the program package TOPAS 4.2 (Bruker) to determine the lattice parameters and average crystallite size by use of the Scherrer equation.^[41] The patterns of Sb₂S₃ (stibnite, #73-0393), Sb₂Se₃ (#75-1462) and Sb (#35-0732) from the ICDD database were used as reference. For each Rietveld refinement, the instrumental correction as determined with a standard powder sample LaB₆ from NIST (National Institute of Standards and Technology) as standard reference material (SRM 660b; a(LaB₆)=4.15689 Å) was taken into account.

Supporting Information. ¹H and ¹³C NMR data and DSC pictures of single source precursors **1** - **4**, powder X-ray diffractograms of Sb₂S₃ and Sb₂Se₃, lattice parameters, density, crystallite size and microstrain of synthesized pure Sb₂S₃, Sb₂Se₃ and substituted Sb₂(S,Se)₃ phases as determined by the Rietveld refinement as well as debyeograms of Sb₂S₃ and Sb₂Se₃ as obtained with **1** - **4** are given in the electronic supplement.

Acknowledgements

S. Schulz gratefully acknowledges financial support by the Mercator Research Center Ruhr (MERCUR) and the Deutsche Forschungsgemeinschaft DFG within the priority program SPP 1708.

Keywords: Metal chalcogenide • nanoparticles • single source precursors

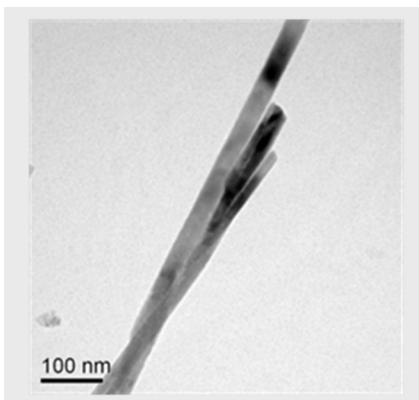
- [1] a) J. A. Chang, J. H. Rhee, S. H. Im, Y. H. Lee, H.-J. Kim, S. I. Seok, M. K. Nazeeruddin, M. Grätzel, *Nano Lett.* **2010**, *10*, 2609-2612; b) S. H. Im, C.-S. Lim, J. A. Chang, Y. H. Lee, N. Maiti, H.-J. Kim, M. K. Nazeeruddin, M. Grätzel, S. I. Seok, *Nano Lett.* **2011**, *11*, 4789-4793; c) N. Maiti, S. H. Im, C.-S. Lim, S. I. Seok, *Dalton Trans.* **2012**, *41*, 11569-11572.
- [2] J. Grigas, *Microwave dielectric spectroscopy of ferroelectrics and related materials*, Gordon and Breach Publishers: Amsterdam, **1996**, Vol. 9.
- [3] a) A. Gruverman, A. Kholkin, *Rep. Prog. Phys.* **2006**, *69*, 2443-2474; b) W. Lee, H. Han, A. Lotnyk, M. A. Schubert, S. Senz, M. Alexe, D. Hesse, S. Baik, U. Gösele, *Nat. Nano* **2008**, *3*, 402-407; c) J. Grigas, *Ferroelectrics* **1978**, *20*, 173-175.
- [4] a) D. Y. W. Yu, H. E. Hoster, S. K. Batabyal, *Sci. Rep.* **2014**, *4*, 4562; b) P. V. Prikhodchenko, J. Gun, S. Sladkevich, A. A. Mikhaylov, O. Lev, Y. Yan Tay, S. K. Batabyal, D. Y. W. Yu, *Chem. Mater.* **2012**, *24*, 4750-4757; c) D. Y. W. Yu, P. V. Prikhodchenko, C. W. Mason, S. K. Batabyal, J. Gun, S. Sladkevich, A. G. Medvedev, O. Lev, *Nat. Commun.* **2013**, *4*, 2922-2928.
- [5] R. Bin Yang, J. Bachmann, E. Pippel, A. Berger, J. Woltersdorf, U. Gösele, K. Nielsch, *Adv. Mater.* **2009**, *21*, 3170-3174.
- [6] L. G. Gribnyak, T. B. Ivanova, *Inorg. Mater.* **1987**, *23*, 478-482.
- [7] N. S. Platakis, H. C. Gatos, *Phys. Stat. Sol.* **1972**, *13*, K1-K4.
- [8] a) S. Messina, M. T. S. Nair, P. K. Nair, *J. Electrochem. Soc.* **2009**, *156*, H327-H332; b) A. M. Fernandez, M. G. Merino, *Thin Sol. Films* **2000**, *366*, 202-206; c) F. T. F. O'Mahony, U. B. Cappel, N. Tokmoldin, T. Lutz, R. Lindblad, H. Rensmo, S. A. Haque, *Angew. Chem. Int. Ed.* **2013**, *52*, 12047-12051; d) S. Messina, M. T. S. Nair, P. K. Nair, *J. Electrochem. Soc.* **2009**, *156*, H327-H332.
- [9] P. Arun, A. G. Vedeshwar, N. C. Mehra, *J. Phys. D* **1999**, *32*, 183-190.
- [10] a) A. J. Minnich, M. S. Dresselhaus, Z. F. Ren, G. Chen, *Energy Environ. Sci.* **2009**, *2*, 466-479; b) M. S. Dresselhaus, G. Chen, M. Y. Tang, R. G. Yang, H. Lee, D. Z. Wang, Z. F. Ren, J. P. Fleurial, P. Gogna, *Adv. Mater.* **2007**, *19*, 1043-1053.
- [11] a) L. G. Gribnyak, T. B. Ivanova, *Inorg. Mater.* **1987**, *23*, 478-482; b) B. R. Chakraborty, B. Ray, R. Bhattacharya, A. K. Dutta, *J. Phys. Chem. Solids* **1980**, *41*, 913-917.
- [12] a) D. M. Rowe in *Thermoelectrics Handbook: Macro to nano*, CRC Press: Boca Raton, FL, **2005**; b) G. S. Nolas, J. Sharp, H. J. Goldsmid, in *Thermoelectrics: Basic principles and new materials developments*, Springer: New York, **2001**; c) D. M. Rowe in *CRC handbook of thermoelectrics*, CRC Press: Boca Raton, FL, **1995**.
- [13] X. W. Zheng, Y. Xie, L. Y. Zhu, X. C. Jiang, Y. B. Jia, W. H. Song, Y. P. Sun, *Inorg. Chem.* **2002**, *41*, 455-461.
- [14] A. I. Boukai, Y. Bunimovich, J. Tahir-Kheli, J. K. Yu, W. A. Goddard, J. R. Heath, *Nature* **2008**, *451*, 168-171.
- [15] R. J. Mehta, Y. Zhang, C. Karthik, B. Singh, R. W. Siegel, T. Borca-Tasciuc, G. Ramanath, *Nature* **2012**, *11*, 233-240.
- [16] R. J. Mehta, C. Karthik, W. Jiang, B. Singh, Y. Shi, R. W. Siegel, T. Borca-Tasciuc, G. Ramanath, *Nano Lett.* **2010**, *10*, 4417-4422.
- [17] D. Li, X. Y. Qin, Y. F. Liu, N. N. Wang, C. J. Song, R. R. Sun, *RSC Adv.* **2013**, *3*, 2632-2638.
- [18] Y. Zhang, R. J. Mehta M., Belley, L. Han, G. Ramanath, T. Borca-Tasciuc, *Appl. Phys. Lett.* **2012**, *100*, 193113-193115.
- [19] Z. Lu, L. P. Tan, X. Zhao, M. Layani, T. Sun, S. Fan, Q. Yan, S. Magdassi, H. H. Hng, *J. Mater. Chem. C* **2013**, *1*, 6271-6277.
- [20] M. K. Han, S. Kim, H.-Y. Kim, S.-J. Kim, *RSC Adv.* **2013**, *3*, 4673-4679.
- [21] Y. Min, J. W. Roh, H. Yang, M. Park, S. Il Kim, S. Hwang, S. M. Lee, K. H. Lee, U. Jeong, *Adv. Mater.* **2013**, *25*, 1425-1429.
- [22] a) Y. Zhang, G. D. Stucky, *Chem. Mater.* **2014**, *26*, 837-848; b) R. J. Mehta, C. Karthik, B. Singh, R. Teki, T. Borca-Tasciuc, G. Ramanath, *ACS Nano*, **2010**, *4*, 5055-5060; c) R. Benoit, V. Hornebecq, F. Weill, L. Lecren, X. Bourrat, M. Tréguer-Delapierre, *J. Mater. Chem. A*, **2013**, *1*, 14221-14226.
- [23] a) R. Bin Yang, J. Bachmann, M. Reiche, J. W. Gerlach, U. Gösele, K. Nielsch, *Chem. Mater.* **2009**, *21*, 2586-2588; b) R. Bin Yang, J. Bachmann, E. Pippel, A. Berger, J. Woltersdorf, U. Gösele, K. Nielsch, *Adv. Mater.* **2009**, *21*, 3170-3174; c) H. F. Bao, X. Q. Cui, C. M. Li, Q. L. Song, Z. S. Lu, J. Guo, *J. Phys. Chem. C* **2007**, *111*, 17131-17135.
- [24] G. Shen, D. Chen, K. Tang, X. Jiang, Y. Qian, *J. Cryst. Growth* **2003**, *252*, 350-354.
- [25] a) Z. Deng, M. Mansuripur, A. J. Muscat, *Nano Lett.* **2009**, *9*, 2015-2020; b) Y. Yu, R. H. Wang, Q. Chen, L.-M. Peng, *J. Phys. Chem. B* **2006**, *110*, 13415-13419; c) J. Ma, Y. P. Wang, Y. J. Wang, P. Peng, J. B. Lian, X. C. Duan, Z. F. Liu, X. D. Liu, Q. Chen, T. Kim, G. Yao, W. J. Zheng, *Cryst. Eng. Comm.* **2011**, *13*, 2369-2374; d) W. Tao, J. Wang,

- D. Wu, J. Chang, F. Wang, Z. Gao, F. Xu, K. Jiang, *Dalton Trans.* **2013**, 42, 11411-11417; e) H. Zhang, M. Ge, L. Yang, Z. Zhou, W. Chen, Q. Li, L. Liu, *J. Phys. Chem. C* **2013**, *117*, 10285-10290.
- [26] X. Wang, K. Cai, H. Liu, *Cryst. Growth Des.* **2011**, *11*, 4759-4767.
- [27] J. Varghese, S. Barth, L. Keeney, R. W. Whatmore, J. D. Holmes, *Nano Lett.* **2012**, *12*, 868-872.
- [28] R. Jin, G. Chen, C. Yan, D. Chen, H. Xu, J. Pei, *Cryst. Eng. Comm.* **2012**, *14*, 8547-8553.
- [29] R. B. Yang, J. Bachmann, E. Pippel, A. Berger, J. Woltersdorf, U. Gösele, K. Nielsch, *Adv. Mater.* **2009**, *21*, 3170-3174.
- [30] J. R. Castro, K. C. Molloy, Y. Liu, C. S. Lai, Z. Dong, T. J. White, E. R. T. Tiekink, *J. Mater. Chem.* **2008**, *18*, 5399-5405.
- [31] a) M. Bochmann, X. Song, M. B. Hursthouse, A. Karaulov, *J. Chem. Soc., Dalton Trans.* **1995**, 1649-1652; b) H.-W. Chang, B. Sarkar, C. W. Liu, *Cryst. Growth Des.* **2007**, *7*, 2691-2695; c) W. Lou, M. Chen, X. Wang, W. Liu, *Chem. Mater.* **2007**, *19*, 872-878.
- [32] G. Gupta, J. Kim, *Dalton Trans.* **2013**, 42, 8209-8211.
- [33] S. Schulz, S. Heimann, J. Friedrich, M. Engenhorst, G. Schierning, W. Assenmacher, *Chem. Mater.* **2012**, *24*, 2228-2234.
- [34] G. Bendt, S. Schulz, S. Zastrow, K. Nielsch, *Chem. Vap. Deposition* **2013**, *19*, 235-241.
- [35] H. Scherrer, S. Scherrer in *Thermoelectrics Handbook, Macro to Nano*, Ed. D.M. Rowe, Francis & Taylor group, Boca Raton, Florida, **2006**, Chapter 27.
- [36] L. W. da Silva, M. Kaviany, C. Uher, *J. Appl. Phys.* **2005**, *97*, 114903-114910.
- [37] S. Zastrow, J. Gooth, T. Boehnert, S. Heiderich, W. Toellner, S. Heimann, S. Schulz, K. Nielsch, *Semicond. Sci. Technol.* **2013**, *28*, 035010-6.
- [38] H. A. Meinema, H. F. Martens, J. G. Noltes, *J. Organomet. Chem.* **1973**, *51*, 223-230.
- [39] S. Heimann, D. Bläser, C. Wölper, R. Haack, G. Jansen, S. Schulz, *Dalton Trans.*, **2014**, 43, 14772-14777.
- [40] P. A. Stadelmann, *EMS—a software package for electron-diffraction analysis and HREM image simulation in materials science, Ultramicroscopy* **1987**, *21*, 131-145.
- [41] H. P. Klug, L. E. Alexander, *X-ray Diffraction Procedures for Polycrystalline and Amorphous Materials*, second ed., Wiley, New York 1974.
- [42] S. Heimann, S. Schulz, D. Bläser, C. Wölper, *Eur. J. Inorg. Chem.* **2013**, 4909-4915.
- [43] H. J. Breunig, H. Jawad, *J. Organomet. Chem.* **1984**, *211*, 257-260.
- [44] C. Löwig, E. Schweizer, *Liebigs Ann. Chem.* **1850**, *75*, 315-355.
- [45] a) A. Hantzsch, H. Hibbert, *Ber. Dtsch. Chem. Ges.* **1907**, *40*, 1508-1519; b) W. J. Lile, R. C. Menzies, *J. Chem. Soc.* **1950**, 617-621; c) J. Pebler, F. Weller, K. Dehnicke, *Z. Anorg. Allg. Chem.* **1982**, *492*, 139-147.
- [46] H. J. Breunig, H. Jawad, *Z. Naturforsch., B: Chem. Sci.* **1982**, *37b*, 1104-1108.
- [47] E. Diemann, *Z. Anorg. Allg. Chem.* **1977**, *433*, 242-246.
- [48] D. Wang, C. Song, X. Fu, X. Li, *J. Cryst. Growth* **2005**, *281*, 611-615.
- [49] K. H. Park, J. Choi, H. J. Kim, J. B. Lee, S. U. Son, *Chem. Mater.* **2007**, *19*, 3861-3863.
- [50] R. Caracas, X. Gonze, *Phys. Chem. Minerals* **2005**, *32*, 295-300.
- [51] G.-Y. Chen, B. Dneg, G.-B. Cai, T.-K. Zhang, W.-F. Dong, W.-X. Zhang, A.-W. Xu, *J. Phys. Chem. C* **2008**, *112*, 672-679.
- [52] ICSD651518: O. M. Aliev, E. V. Magerramov, P. G. Rustamov, *Russ. J. Inorg. Chem. (Z. Neorgan. Khimii)* **1977**, *22*, 1539-1541.
- [53] J. Lee, A. Berger, L. Cagnon, U. Gösele, K. Nielsch, J. Lee, *Phys. Chem. Chem. Phys.* **2010**, *12*, 15247.
- [54] E. A. El-Sayad, *J. Non-Cryst. Solids* **2008**, *354*, 3806-3811.
- [55] A. M. Moustafa, E. A. El-Sayed, *Egypt. J. Solids* **2009**, *32*, 71-80; b) ICSD-650812: N. K. Abrikosov, V. I. Ivlieva, *Izv. Akad. Nauk, Neorg. Mater.* **1968**, *4*, 763-766.

Entry for the Table of Contents

FULL PAPER

Binary Sb_2S_3 and Sb_2Se_3 nanowires as well as ternary $\text{Sb}_2(\text{S,Se})_3$ nanowires were synthesized by thermal decomposition of four novel single source precursor of the type $(\text{Et}_2\text{Sb})_2\text{E}$ and Et_3SbE ($\text{E} = \text{S, Se}$) in the presence of suitable capping agents and characterized by XRD, REM, EDX, ED and HRTEM.



*Stefan Heimann, Wilfried Assenmacher, Oleg Prymak, and Stephan Schulz**

Page No. – Page No.

Synthesis of binary Sb_2E_3 ($\text{E} = \text{S, Se}$) and ternary $\text{Sb}_2(\text{S,Se})_3$ Nanowires using *tailor-made* Single-Source-Precursors

DuEPublico

Duisburg-Essen Publications online

UNIVERSITÄT
DUISBURG
ESSEN

Offen im Denken

ub | universitäts
bibliothek

This text is made available via DuEPublico, the institutional repository of the University of Duisburg-Essen. This version may eventually differ from another version distributed by a commercial publisher.

DOI: 10.1002/ejic.201500325

URN: urn:nbn:de:hbz:464-20201125-111856-0

This is the **peer reviewed version** of the following article: *Eur. J. Inorg. Chem.* 2015, 14, 2407-2415, which has been published in final form at:
<https://doi.org/10.1002/ejic.201500325>

All rights reserved.